ELSEVIER

journal of MEMBRANE SCIENCE

Special Issue: Membranes for a Sustainable Future

Available online at www.sciencedirect.com

ScienceDirect

The Journal is Endorsed by

nams

The role of partial crystallinity on hydrogen permeation in Fe–Ni–B–Mo based metallic glass membranes

Kyle Brinkman [a],*, Elise Fox [a], Paul Korinko [a], David Missimer [a], Thad Adams [a], Dong Su [b]

[a] Savannah River National Laboratory, Aiken, SC 29808, USA
[b] Brookhaven National Laboratory, Upton, NY 11973, USA

ARTICLE INFO

ABSTRACT

A potentially exciting material for membrane separations are metallic glass materials due to their low cost, high elastic toughness and resistance to hydrogen embrittlement as compared to crystalline Pd-based membrane systems. However, at elevated temperatures and extended operation times structural changes including partial crystallinity may appear in these amorphous metallic systems. This study reports on the investigation of time and temperature dependent crystalline phase formation in conjunction with in situ crystallization/hydrogen permeation experiments at elevated temperatures. At temperatures near 400 °C a FeNi crystalline phase appears as 22 vol.% inside the host amorphous matrix and the resulting composite structure remains stable over 3 h at temperature. The hydrogen permeation at 400 °C of the partially crystalline material is similar to the fully amorphous material near 5×10^{-9} mol H_2/m s $Pa^{1/2}$, while ambient temperature electrochemical permeation at 25 °C revealed an order of magnitude decrease in the permeation of partially crystalline materials due to differences in the amorphous versus crystalline phase activation energy for hydrogen permeation.

© 2011 Elsevier B.V. All rights reserved.

1. Introduction

Membranes based on amorphous metals are an emerging technology for gas separations in syngas and reforming processes with significant potential to overcome challenges associated with existing membranes based on crystalline metals [1]. Amorphous metals have recently demonstrated remarkable mechanical [2] and catalytic properties [3] for use in structural materials and electrochemical devices for energy conversion. Metallic glasses are intrinsically suitable for membranes due to their atomic level porous structure, excellent mechanical properties, and the lack of any microstructure defects such as grain boundaries and dislocations [4]. Furthermore, they have demonstrated flexibility in processing methodology which may ease the transition from lab scale membranes to industrial production. One of the major drawbacks to the industrial use of Pd–Pd/alloy membranes is that during cycling above and below a critical temperature an irreversible change takes place in the palladium lattice structure which can result in significant damage to the membrane [5]. Furthermore, the cost associated with Pd-based membranes is a potential detractor for their continued use and

bulk metallic glass alloys offer a potentially attractive alternative.

Several metallic glass compositions have been shown to possess high permeation rates comparable to those measured for pure Pd metal [1,6,7]. Both of these properties – high permeation and high strength/toughness potentially make these materials attractive for gas separation membranes that could resist hydrogen embrittlement. Nickel- and iron-refractory metal type alloys have shown high liquidius ($T_L \sim 1300$–1500 °C) temperatures, elevated glass forming temperatures ($T_g \sim 650$ °C) to ensure durable operation in the high-temperature membrane separations [8]. In addition, they have demonstrated appreciable levels of hydrogen permeability of 5.3×10^{-9} mol H_2/m s $Pa^{1/2}$ for the 2826 alloy at 400 °C and 700 Torr pressure differential compared to Pd flux of 2×10^{-8} mol H_2/m s $Pa^{1/2}$ [9–11]. However, a fundamental understanding of the relationship between partially crystalline structure/devitrification and permeation/embrittlement in these materials is required in order to determine the operating window for separation membranes and provide additional input to material synthesis community for improved alloy design. This work aims to fill the knowledge gap regarding the impact of crystallization on the hydrogen permeation properties of Fe–Ni–B–Mo based materials, specifically alloy 2826.

The permeation of hydrogen through metallic membranes is a multi-function process involving adsorption, dissociation, diffusion, and recombination and desorption [12]. Two of the inherent

* Corresponding author. Tel.: +1 803 725 9843.
  E-mail addresses: kyle.brinkman@srnl.doe.gov, kylesbrinkman@yahoo.com
(K. Brinkman).

materials properties that play a critical role in these processes are the solubility and diffusivity of hydrogen in the material. Though the long range structure is disordered in amorphous materials, diffusion has been thought to occur through interstitial mechanisms similar to crystalline materials [13]. The solubility however, should be enhanced in amorphous materials due to the greater density of defects and distribution of sorption sites which can be occupied by hydrogen over a wide range of potential energies [14]. For materials which are partially crystalline one of the critical factors determining the diffusivity, solubility and ultimately the permeability is the role the secondary crystalline phase play in the composite structure [15]. It has also been shown that the nature of the crystalline phase depends on the gas environment of crystallization or hydrogen content of the material [16,17]. The hydrogen permeability of melt-spun alloys based of the form $Zr_{65}Al_{7.5}Ni_{10}Cu_{12.5}Pd_5$ was examined as a function of microstructure ranging from glassy, quasi-crystalline particles dispersed in the glassy state and fully crystalline state [15]. The hydrogen permeability of the alloy was highest in the amorphous state and lowest in the crystalline state. Recently, predictions based on first principles calculations on model Fe_3B metallic glass systems revealed that hydrogen solubility in the amorphous and crystalline materials should differ by orders of magnitude under conditions relevant to practical membrane separations unit operations [18]. However, there is little experimental data available on the structure/property relations of crystallization and permeation in iron boron based metallic glass systems.

In order to experimentally study the impact of partial crystallization on the crystalline structure and subsequent impact on permeation, in situ high temperature X-ray diffraction analysis was performed as a function of temperature and gas composition coupled with select post annealing TEM analysis. Finally, hydrogen permeation properties were measured in two measurement modes: (i) in situ where crystallization took place during gas phase hydrogen permeation at elevated temperatures and (ii) ex situ where pre-crystallized sample's hydrogen permeation properties were measured and compared with the as-received amorphous materials at ambient temperature using an electrochemical method.

2. Experimental

Metallic glass samples of iron boron based composition 2826 with a nominal thickness of 25 μm in 2 in. wide ribbons were purchased from commercial sources (MetGlas Inc., Conway, SC) with the nominal compositions given as: Fe (40–50%), B (1–5%), Mo (5–10%), Co (0.3%), and Ni (40–50%). Metglass ribbon samples were heated under vacuum to elevated temperatures for various times and quenched under argon to achieve different degrees of partial crystallinity. Samples were initially characterized from 10 to 90 degrees two theta on a PanAnalytical X-ray diffractometer in order to confirm the absence of detectable crystallization in the as-received baseline samples. Samples which were intentionally crystallized were characterized by X-ray diffraction (XRD) to determine the degree of crystallinity. In situ XRD at elevated temperature from 25 to 710 °C using a high temperature Anton Paar HTK 1200 stage in flowing air, He and He 96%, H_2 4% mixtures was performed. A 651 model TA Instruments DSC was used to evaluate crystallization temperatures at scan rates of 10 °C/min from 25 °C up to 590 °C in argon and 4% hydrogen 96% argon gas flowing at 30 sccm. The instrument was temperature calibrated using an indium metal standard and the nominal metallic glass sample mass was ~8 mg.

Gas phase permeation test samples were sealed by crimping between two VCR fittings (Swagelock) with a Ag plated Cu gasket

which were then connected to a standard 2.12″ conflat flange (CF) and helium leak tested to confirm lower than 1×10^{-7} std cm^3/s at 1 atmosphere pressure. Measurement of the steady state permeation flux was conducted under sub-atmospheric pressures (400–700 Torr), values typically used at the Savannah River Site for hydrogen isotope purification. The slope of the saturation data in Torr/s can be converted into mol H_2/s via the ideal gas equation $PV = nRT$ with the known expansion volume of the system. The flux J is then given by Eq. (1)

$$J = \frac{K}{A \times P^{1/2}} \tag{1}$$

where J = hydrogen flux (mol/m^2 s Pa$^{1/2}$), K = slope dP/dt in (mol/s), A = permeation area (m^2), and P = feed pressure in Pascal (Pa).

The ambient temperature hydrogen gas permeation properties were investigated using an electrochemical hydrogen permeation setup based on the ASTM G148-7 [6,19]. A 0.1 M NaOH solution was used with platinum counter electrodes and standard calomel reference electrodes (SCE). Cathode charging currents were varied from -0.1 mA/cm^2 to -7 mA/cm^2 with anode detection potential fixed at 200 mV (SCE). The area available for permeation was 3.12 cm^2. After establishing a stable baseline, the initiation of cathode charging leads to an increase in the anode current which is proportional to the hydrogen flux (mol/m^2 s) through the membrane described in Eq. (2)

$$Jss = \frac{J/A}{F} \tag{2}$$

where Jss = steady state flux (mol/m^2 s), J = steady state current (A), A = permeation area (m^2), and F = Faraday's constant, 9.6×10^4 C/mol.

The hydrogen permeation rate (mol/m s) is obtained by the product of Jss with the sample thickness as described in Eq. (3)

$$P = Jss \times L \tag{3}$$

where P = hydrogen permeation rate (mol/m s) and L = sample thickness 25×10^{-6} m (25 μm).

3. Results

3.1. Crystallization behavior (XRD/DSC)

Differential scanning calorimetry (DSC) was performed on as-received samples at a ramp rate of 10 °C/min under argon atmosphere (30 sccm) from 25 °C to 590 °C for the determination of baseline crystallization behavior. Table 1 summarizes the crystallization temperature as determined from the peak of exotherm and nominal composition for 2826 and three other commercially available iron based alloys (2605S3A, 2714A 2605 SA1). The percent crystallinity was determined from XRD scans incorporating two assumptions: (i) the initial metallic glass is amorphous, i.e., it does not have any crystallinity and (ii) the full width half max (FWHM) of the amorphous component is constant. The amorphous "hump" in the 25 °C HTXRD scans were profile fitted using the pseudovoight (combination Gaussian and Lorentzian) function to determine their full width half maximum (FWHM). The FWHM for the amorphous reflection in the apparently non-crystalline scans up to ~300 °C (H_2/He and air) or 350 °C (He) was also measured and had the same relative value as the 25 °C run indicating crystallization had not yet occurred. Using this FWHM, the integrated area for the amorphous component in the remaining crystalline scans was determined. The percent crystallinity was calculated using the simple relationship: % crys = 100 × (total peak area − amorphous area)/total peak area. An example of this amorphous fraction fitting process is shown in Fig. 1 [20].

Table 1
Crystallization temperatures determined by differential scanning calorimetry (DSC) and nominal compositions.

Alloy	T_1 cryst (°C)	Fe	B	Cr	Mo	Co	Ni	Si
2826	421	40–50%	1–5%	0%	5–10%	0.3%	40–50%	0%
2605S3A	521	85–95%	1–5%	1–5%	0%	0%	0%	1–5%
2714A	551	7–13%	1–5%	0%	0%	75–90%	1–5%	7–13%
2605SA1	504	85–95%	1–5%	0%	0%	0.2%	0.2%	5–10%
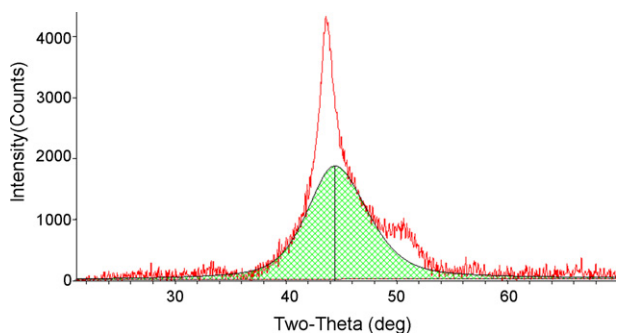
Fig. 1. X-ray diffraction (XRD) spectra of 2826 metallic glass material at 400 °C in He. Shaded region is profile fitting of the amorphous portion with remaining area representing the crystalline content.
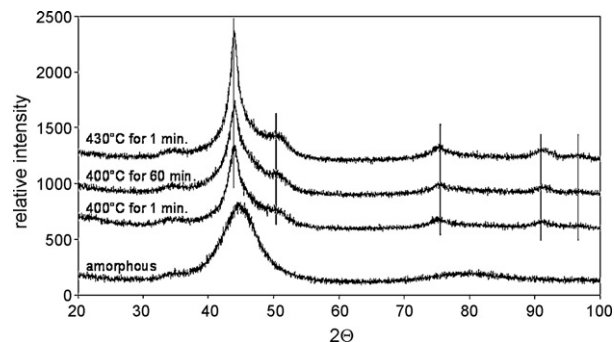
Fig. 2. X-ray diffraction (XRD) of as-received amorphous 2826 metglass material and samples after annealing 400 °C for 1 min and 1 h, 430 °C for 1 min showing increased level of crystallinity.

Fig. 2 shows the XRD patters of as-received 2826 samples compared to samples that were annealed to 400 °C and 430 °C for 1 min and 400 °C for 1 h followed by and a furnace quench under argon atmosphere. The crystalline fraction was found to increase with time at 400 °C and was identified as FCC $Fe_{0.5}Ni_{0.5}$, an alloy with an ordered tetragonal superlattice (a = 2.53 Å, c = 3.58 Å). Fig. 3 shows the TEM and selected area diffraction (SAD) patterns of the as-

received and annealed samples (400 °C and 430 °C for 1 min and 400 °C for 1 h). Firstly, Fig. 3a displays an amorphous diffraction pattern confirming the assumption that the as-received samples had no crystallinity present. At temperatures of 400 and 430 °C crystalline phases are evident however there is a distinct amorphous phase present between the grains even after an annealing duration of 1 h at 400 °C. Fig. 4 shows the high resolution TEM images
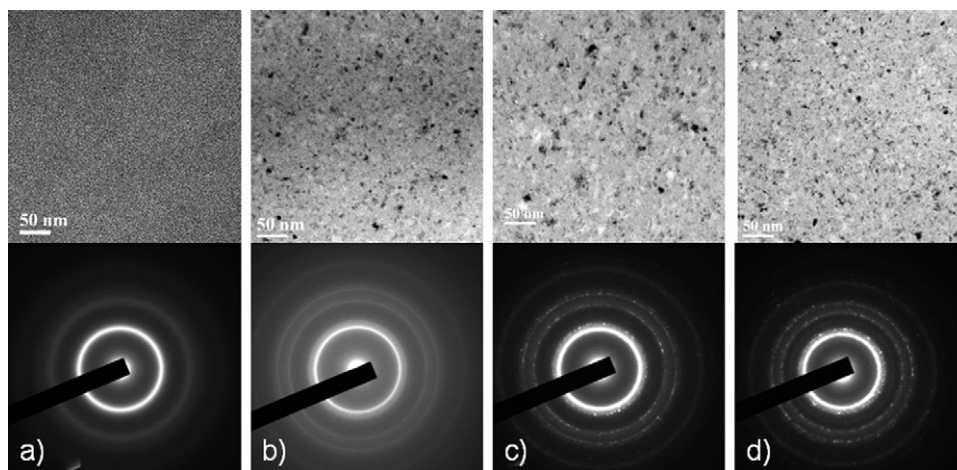
Fig. 3. TEM images at a magnification of 60,000× and corresponding selected area diffraction pattern (SAD) of (a) as-received amorphous 2826 metglass material and samples after annealing, (b) 400 °C for 1 min, (c) 400 °C for 1 h and (d) 430 °C for 1 min showing increased level of crystallinity.
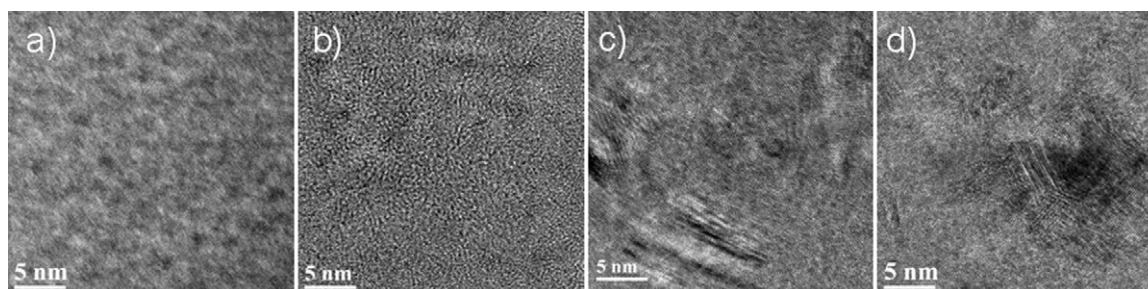
Fig. 4. TEM high resolution image at 800,000× magnification displaying twin crystalline structures with the onset of crystallization in (c) and (d).

Table 2
TEM determined grain size and chemical compositions from EDAX.

Sample	Grain size (nm)	Fe	Mo	Ni
As-received	0	48.71	1.75	46.50
400 °C 1 min	2–8	49.34	2.17	47.87
400 °C 1 h	4–15	48.36	5.39	44.48
430 °C 1 min	6–16	47.69	4.55	46.23

taken at 800 K magnification. Twin structures are known to form as a way to relax strain that occurs with concomitant crystallization and coarsening. In the present case, twins were observed in Fig. 4(c) and (d) which appeared rapidly with the onset of crystallization and a grain/crystalline size in the 15 nm range. Table 2 summarizes the TEM results of grain size and chemical composition. The compositions all fall within the nominal alloy composition cited in Fig. 1 with the exception of the Mo which was unusually low in the as-received sample. It is speculated that there were differences in the amorphous versus crystalline Mo sputter/damage which resulted from TEM preparation using ion milling.

High temperature XRD under various gas environments was employed in order to map the crystallization behavior over conditions of interest to membrane separations. Figs. 5–7 displays the temperature dependence of crystalline phase formation in He, 4%H$_2$/He and air environments respectively. A summary of these experiments is included in Table 3. Confirming the results obtained from DSC and XRD spectra of furnace quench experiments detailed in the previous section, the equimolar binary Fe/Ni alloy, tetrataenite [21], was the first crystalline phase to appear at 400 °C in 2826 heated in all three gases. This composition is consistent with the initial glass chemistry, which is approximately 50:50 Fe/Ni. In contrast annealing under air resulted in the, iron being gradually removed through oxidation from the glass to form iron borates and hematite, leaving only Ni metal in the residue. This is expected since the free energy of formation for iron oxides is more negative than for NiO [22]. At higher temperatures Ni was not detected in the XRD patterns, since it was obscured by the thick oxide coatings and was only identified in the pulverized HTXRD residue.

The second phase, Fe$_{11.5}$Ni$_{11.5}$B$_6$ [23], formed at 450 or 500 °C immediately after tetrataenite crystallization and was found to be stable in He and H$_2$/He up to 710 °C. In air it survived only to 550 °C, after which it was completely oxidized to iron oxide borate and iron borate. An additional possibility for these XRD reflections is an isostructural molybdenum containing phase, (Fe,Ni,Mo)$_{23}$B$_6$ [24],
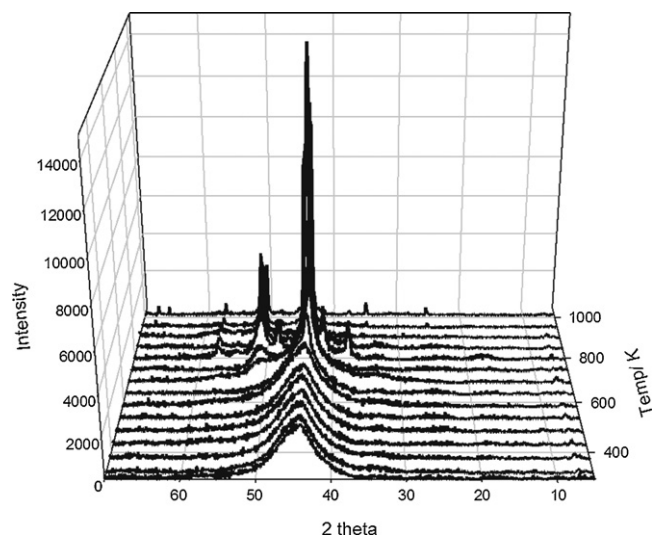
Fig. 6. High temperature X-ray diffraction (HTXRD) in 4% hydrogen, balance helium gas environment from 25 °C to 710 °C.

which is indistinguishable by XRD from Fe$_{11.5}$Ni$_{11.5}$B$_6$. The stoichiometry of the "true" boride phase is probably similar to the Fe, Ni, and, Mo molar ratio in the initial glass. The final non-oxide, Mo$_2$FeB$_2$ [25] or possibly Mo$_2$FeB$_4$ [26], was found only in the HTXRD residues at concentrations, which are too low for detection.

3.2. Permeation

The steady state gas permeation measurements of the as-received 2826 alloy at 350 and 400 °C are shown in Fig. 8 displaying the pressure versus time. The hydrogen permeability calculated from Eq. (1) was 5.3×10^{-9} mol H$_2$/m s Pa$^{1/2}$ for the 2826 alloy at 400 °C and 700 Torr pressure differential compared to Pd flux of 2×10^{-8} mol H$_2$/m s Pa$^{1/2}$. Similar experiments with a commercially available high iron content alloy 2605 resulted in gas phase permeation of 2.5×10^{-9} mol H$_2$/m s Pa$^{1/2}$ at 400 °C and 700 Torr feed pressure [27]. In addition to steady-state gas phase measurements, "dynamic" measurement techniques were used for in situ crystallization/permeation experiments. Fig. 9 shows a plot of measured total pressure and hydrogen partial pressure versus time and temperature for a 2826 metglass alloy. In the dynamic measure-
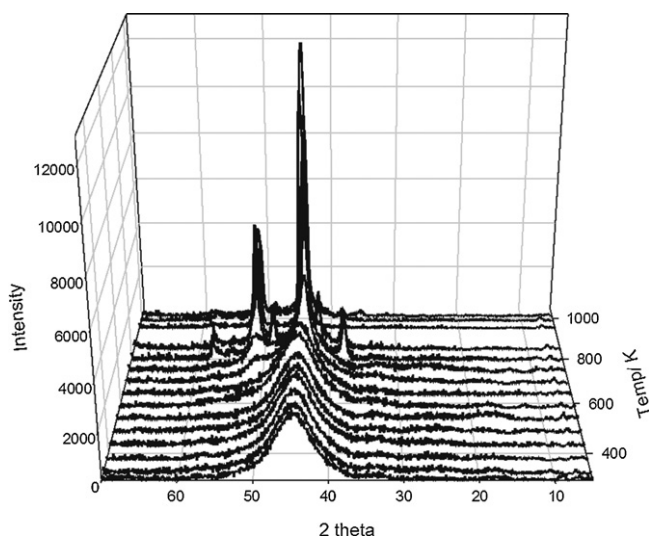
Fig. 5. High temperature X-ray diffraction (HTXRD) in helium gas environment from 25 °C to 710 °C.
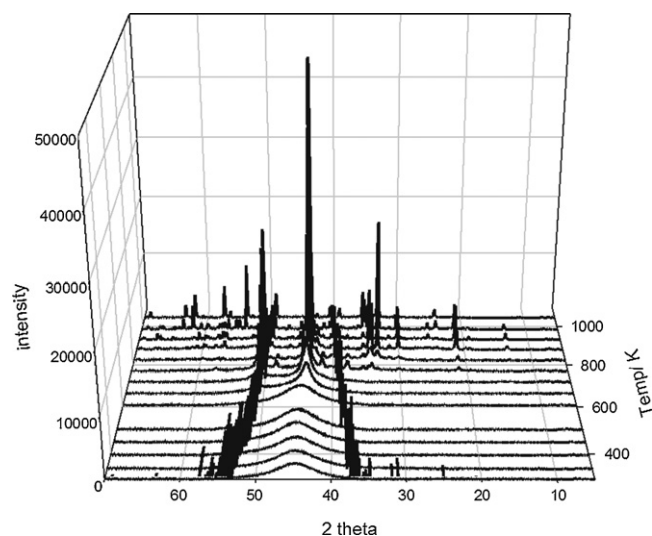
Fig. 7. High temperature X-ray diffraction (HTXRD) in air from 25 °C to 710 °C.

Table 3
Summary of identified phases for 2826 metallic glass crystallization experiments.

Compound	Formula	5°/min in He (°C)	5°/min in 4% H_2 in He (°C)	5°/min in air (°C)
Tetrataenite	FeNi	400–710	350–710	350–650
Boron iron nickel	$Fe_{11.5}Ni_{11.5}B_6$	500–710	500–710	450–550
Boron iron molybdenum	Mo_2FeB_2	710	710	
Iron oxide borate	$Fe_2O(BO_3)$			450–710
Iron borate	$Fe(BO_3)$			500–710[a]
Molybdenum iron oxide	Mo_3Fe_3O			500–710
Hematite	Fe_2O_3			650–710
Nickel	Ni			710
Kamiokitei	$Fe_2Mo_3O_8$			710[b]
Sassolite[c]	$B(OH)_3$	Residue only	Residue only	
Isostructural variation of Pinakiolte[c]	$(Mg,Mn)_2Mn(BO_3)_2$	Residue only		

[a] $FeBO_3$ could be present at 710 °C in air. Its presence would be masked by the large hematite peaks.
[b] $Fe_2Mo_3O_8$ was found only in the HTXRD residues at concentrations, which are too low to detect on the high temperature stage. It is assumed that it develops above 500 °C.
[c] Formed during the cool down cycle as air infiltrated the camera.
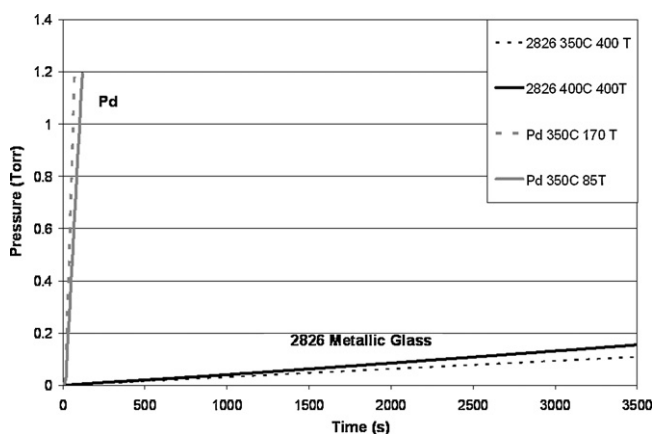
Fig. 8. Pressure (Torr) versus time saturation plot for 2826 metallic glass versus Pd standard. The slope of the pressure versus time plot is proportional to the hydrogen flux through the membrane dP/dt (mol/s), flux in mol/m² s Pa$^{1/2}$ calculated via Eq. (1).

ment configuration, the backside of the membrane is exposed to the turbomolecular pump pressure so that the actual hydrogen flux is proportional to both the pump speed and concentration/partial pressure presented in Fig. 9. Nevertheless, for a relative value of hydrogen permeation in the same sample, the hydrogen partial pressure is a measure of the hydrogen flux. The hydrogen flux is seen to increase with increasing temperature as expected and time dependent deviations will be discussed in the following section.
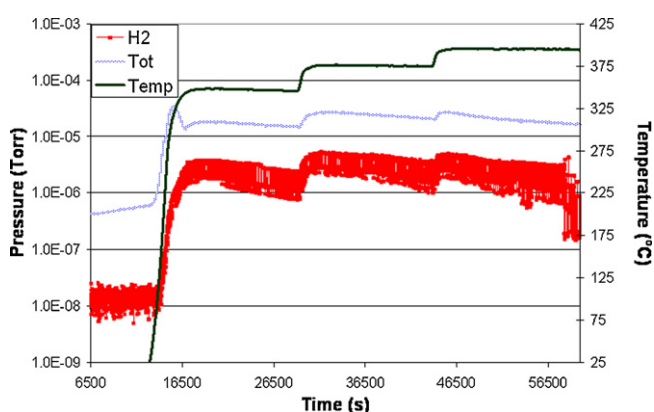
Fig. 9. Pressure in the dynamic hydrogen gas permeation measurement conducted at 350, 380 and 400 °C as a function of time.

The corresponding as-received materials were characterized at ambient temperature using electrochemical permeation techniques and presented in Fig. 10 with a charging sequence of −7, −1 and −0.1 mA/cm². The current measured in Fig. 10 was converted into flux and permeation rate via Eqs. (2) and (3) resulting in values of 3×10^{-11} mol H_2/m s for 2826 alloys measured at 25 °C and −1 mA/cm² charging conditions as compared to 3×10^{-9} mol H_2/m s for Pd metal standard under the same conditions. dos Santos has reported flux values on the order of 1×10^{-8} mol/m s for 150 μm $Pd_{80}Ru_{20}$ alloy under similar charging conditions [28]. Samples were annealed to elevated temperatures, characterized in terms of crystalline nature and then measured at ambient temperatures in the electrochemical permeation setup. Fig. 11 shows the current proportional to the hydrogen flux versus time for an amorphous 2826 and crystalline sample annealed to 430 °C for 1 min showing the near order of magnitude decrease in the current with increasing crystallinity of the membrane.

Electrochemical permeation rates are quoted in mol/m s at given charging conditions, while gas phase measurements are quoted as mol/m s Pa$^{1/2}$. In order to compare electrochemical measurements with gas phase measurements the link between the electromotive force used for H_2 generation and the hydrogen pressure must be established from the Nernst equation:

$$E = \frac{RT}{2F} \ln \frac{pH_{2_I}}{pH_{2_{II}}} \tag{4}$$

where E = electromotive force in volts (V), R is gas constant 8.314 J/molK, F is Faraday's constant, 9.64×10^4 C/mol, pH_2 are the partial pressure of hydrogen on side I and side II of the membrane.
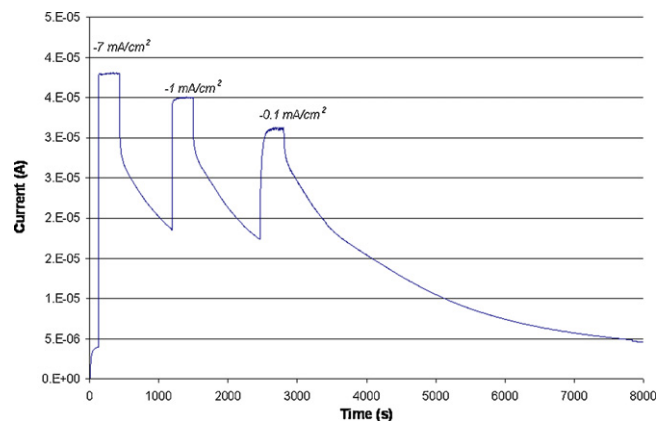
Fig. 10. Electrochemical hydrogen permeation of 2826 metallic glass displaying current (A) proportional to hydrogen flux at the anode versus time (s) for as-received 2826 alloy with charging sequence of −7, −1 and −0.1 mA/cm².

Table 4
Hydrogen permeation summary in partially crystalline versus amorphous 2826 metallic glass samples as compared to Pd, Fe and Ni metallic elements in the temperature range from 120 to 400 °C[29].

Alloy	Electrochemical permeability ($mol\ H_2/m\ s$)	Electrochemical permeability ($mol\ H_2/m\ s\ Pa^{1/2}$)	Gas phase permeability 350–400 °C ($mol\ H_2/m\ s\ Pa^{1/2}$)	Hydrogen flux activation energy (kJ/mol)
Pd	3.5×10^{-9}	1×10^{-10}	2.8×10^{-8a} 7.4×10^{-8b}	25 [29]
2826 amorphous	3×10^{-11}	1×10^{-12}	5.3×10^{-9c}	37
2826 partially crystalline 430 °C 1 min	2.6×10^{-12}	8×10^{-14}	5×10^{-9c}	50
Fe	–	–	2×10^{-10}	44 [29]
Ni	–	–	5×10^{-11}	59 [29]

[a] 400 °C and 700 Torr from Ref. [5].
[b] 350 °C and 170 Torr, this work.
[c] 400 °C and 700 Torr, this work.
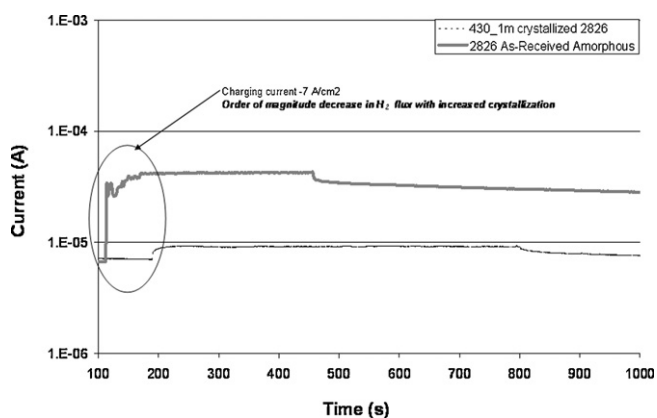
Fig. 11. Electrochemical hydrogen permeation of 2826 metallic glass for amorphous sample and partially crystallized material after annealing at 430 °C for 1 min under charging condition of $-7\ mA/cm^2$ showing a near order of magnitude decrease in the hydrogen flux current with increasing crystallinity of the membrane.

Since the hydrogen diffusing through the membrane is oxidized on side II resulting in the current measured for hydrogen flux, the value of hydrogen partial pressure is very low. For this estimation we assume that the value is 1×10^{-9} bar (or 0.0001 Pa). Using Eq. (4), with charging conditions of ($-1\ mA/cm^2$) and 200 mV applied to the membrane results in an effective pressure differential driving force $\Delta P^{1/2}$ of 31 $Pa^{1/2}$ which converts the as-received 2826 flux of $3 \times 10^{-11}\ mol/m\ s$ into $9.7 \times 10^{-13}\ mol/m\ s\ Pa^{1/2}$. A comparison of the electrochemical and gas phase measurements in the same units for both as-received and partially crystalline 2826 alloy compared with Pd, Fe and Ni metallic elements from literature [29] are presented in Table 4.
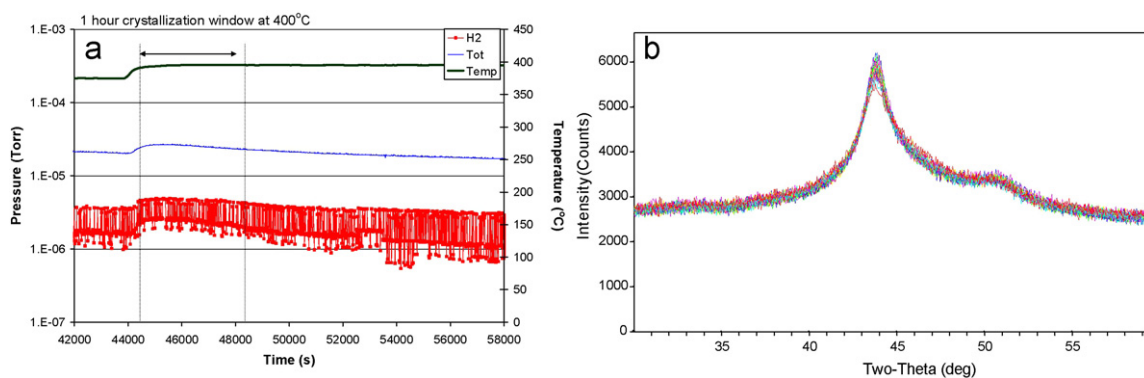
4. Discussion

A close up of the dynamic permeation measurement displaying pressure versus time at 400 °C is shown in Fig. 12a. Inspection of the figure reveals (i) a decrease in the flux with time at 400 °C as well as (ii) a change in the slope of the pressure versus time relation which is proportional to the hydrogen flux. Fig. 12b shows the XRD spectra versus time at 400 °C in a He inert atmosphere. Amorphous versus crystalline content determined from XRD spectra at 400 °C indicted that the crystalline content increased from 17% after 10 min to approximately 28% after 3 h at 400 °C. Kinetic estimates from DSC experiments indicate that the reaction should be complete after approximately 1 h [9,30,31]. However, XRD data show the crystalline content is only 22% after 1 h, and slowly increases to 28% after 3 h time where it remains stable. This behavior can be explained by an "in-complete" phase transformation which consists of stable crystalline phases inside an amorphous matrix. This phenomenon been observed in FeNi metallic glass doped with Co [32] as well as the present work where this type of microstructure is graphically displayed in both Figs. 3 and 4.

This observation of a composite amorphous/crystalline structure can explain the ensemble of structure/property relations observed in the in situ permeation experiments consisting of: (i) a quick crystallization of a small fraction of the material leading to both crystalline content measured in XRD and a reduction in hydrogen flux in permeation experiments and (ii) small changes in crystalline content after the first hour leading to small changes in the XRD crystalline patterns and no measurable difference in hydrogen permeation with time up to 3 h at 400 °C in hydrogen environments. The fact that the material retains significant amount of amorphous content after 3 h at 400 °C is reflected in both the XRD patterns (amorphous hump), as well the observed permeability which would be lower by an order of magnitude in fully crystalline

Fig. 12. (a) Dynamic gas flux measurement of 2826 alloy at 400 °C as a function of time and (b) isothermal XRD scans of 2826 metallic glass acquired over a 3-h period at 400 °C in 4% H_2/96% He.

specimens [29,33]. At lower temperatures (25 °C) near ambient conditions, even partially crystalline 2826 metallic glass displays an order of magnitude decrease in permeability as compared to fully amorphous samples, while at elevated temperatures (400 °C) near membrane operating conditions the permeabilities are essentially the same. This is due to differences in crystalline versus amorphous activation energy for hydrogen permeation shown in Table 4. It is seen that FCC parent metals like Fe and Ni have large activation energies in the range of 44–59 kJ/mol as compared to 25 and 27 for Pd and amorphous 2826 metglass membranes respectively [29]. Therefore, in the microstructures developed in partially crystalline 2826 metglass materials shown in Fig. 3, the permeation properties of the crystalline phase are dominant at lower temperatures.

5. Conclusion

The temperature and composition of crystalline phases were determined by X-ray diffraction under argon, air and hydrogen gas environments. Ex situ experiments revealed that hydrogen permeation was in crystalline samples by an order of magnitude from 3×10^{-11} mol H_2/m s to 2.6×10^{-12} mol H_2/m s in 2826 alloys due to reduced solubility of hydrogen in the crystalline phase. In situ studies on the 2826 alloy revealed a drop in permeation at 400 °C during the first hour (with crystalline content by XRD increasing from 0 to 17%), followed by stabilization of the flux and crystalline content (27%) over a 3-h period. Combined TEM, permeation and XRD analysis used to interpret results based on crystalline phase co-existing in an amorphous matrix.

References

[1] M.D. Dolan, et al., Composition and operation of hydrogen-selective amorphous alloy membranes, Journal of Membrane Science 285 (1–2) (2006) 30–55.
[2] M. Demetriou, et al., A damage-tolerant glass, Nature Materials 10 (2011) 123–128.
[3] M. Carmo, et al., Bulk metallic glass nanowire architecture for electrochemical applications, ACS Nano 5 (4) (2011) 2979–2983.
[4] S. Yamaura, A. Inoue, Effect of surface coating element on hydrogen permeability of melt-spun Ni40Nb20Ta5Zr30Co5 amorphous alloy, Journal of Membrane Science 349 (1–2) (2010) 138–144.
[5] N.W. Ockwig, T.M. Nenoff, Membranes for hydrogen separation, Chemical Reviews 107 (10) (2007) 4078–4110.
[6] T.M. Adams, J. Mickalonis, Hydrogen permeability of multiphase V–Ti–Ni metallic membranes, Materials Letters 61 (3) (2007) 817–820.
[7] J.W. Phair, R. Donelson, Developments and design of novel (non-palladium-based) metal membranes for hydrogen separation, Industrial & Engineering Chemistry Research 45 (16) (2006) 5657–5674.
[8] X.J. Gu, S.J. Poon, G.J. Shiflet, Journal of Materials Research 22 (2007) 344.
[9] K. Brinkman, et al., The impact of partial crystallization on the permeation properties bulk amorphous glass hydrogen separation membranes, Materials Research Society Symposium Proceedings 1126 (2009) S09–13.
[10] G. Alfeld, J. Völkl, Hydrogen in Metals I, Springer-Verlag, New York, 1978.
[11] N.M. Peachey, R.C. Snow, R.C. Dye, Composite Pd/Ta metal membranes for hydrogen separation, Journal of Membrane Science 111 (1) (1996) 123–133.
[12] T.L. Ward, T. Dao, Model of hydrogen permeation behavior in palladium membranes, Journal of Membrane Science 153 (2) (1999) 211–231.
[13] N. Eliaz, D. Fuks, D. Eliezer, A new model for the diffusion behavior of hydrogen in metallic glasses, Acta Materialia 47 (10) (1999) 2981–2989.
[14] J.H. Harris, W.A. Curtin, M.A. Tenhover, Universal features of hydrogen absorption in amorphous transition-metal alloys, Physical Review B 36 (11) (1987) 5784–5797.
[15] S.I. Yamaura, et al., Hydrogen permeation of the Zr65Al7.5Ni10Cu12.5Pd5 alloy in three different microstructures, Journal of Membrane Science 291 (1–2) (2007) 126–130.
[16] N. Ismail, et al., Hydrogenation and its effect on the crystallisation behaviour of Zr55Cu30Al10Ni5 metallic glass, Journal of Alloys and Compounds 298 (1–2) (2000) 146–152.
[17] N. Ismail, et al., Hydrogenation of Zr–Cu–Al–Ni–Pd metallic glasses by electrochemical means, Journal of Alloys and Compounds 480 (2) (2009) 321–324.
[18] S.Q. Hao, M. Widom, D.S. Sholl, Probing hydrogen interactions with amorphous metals using first-principles calculations, Journal of Physics-Condensed Matter 21 (11) (2009) 7.
[19] ASTM G148-97 Standard Practice for Evaluation of Hydrogen Uptake, P., and Transport in Metals by an Electrochemical Technique.
[20] Due to the uncertainty in measuring the integrated areas, the estimated error for the % crystallinity determination is ±10%.
[21] T. Tagai, H. Takeda, T. Fukuda, Superstructure of tetrataenite from the Saint Severin meteorite, Zeitschrift fur Kristallograhie 210 (1995) 14.
[22] HSC Chemistry, Outokumpu Research Oy, Finland, 2009, www.outokumpu.com/hsc.
[23] Y. Khan, Crystallization behaviour of the melt-quenched (Fe$_{1-y}$Ni$_y$)3B alloys, Zeitschrift fur Metallkunde 74 (1983) 385.
[24] E. Kamzeeva, N. Khatanova, G. Zhdanov, Sov. Phys. Crystallogr. (Engl. Transl.) 29 (1984) 338.
[25] W. Rieger, H. Nowotny, F. Benesovsky, Die Kristallstruktur von Mo$_2$FeB$_2$ – Kurze Mitteilung, Monatshefte fur Chemie 95 (1964) 1502.
[26] H. Haschke, H. Nowotny, F. Benesovsky, Investigations of the three component systems: (Mo,W)–(Fe,Co,Ni)–B, Monatshefte fur Chemie 97 (1966) 1459.
[27] K. Brinkman, E. Fox, P. Korinko, Structural Interactions of Hydrogen with Bulk Amorphous Microstructures in Metallic Systems: Understanding the Role of Partial Crystallinity on Permeation and Embrittlement, 2009, SRNS-STI-2008-00133 www.osti.gov.
[28] D.S. dos Santos, S. Miraglia, D. Fruchart, Effects of cathodic charging on hydrogen permeation in a Pd80Rh20 alloy, Journal of Alloys and Compounds 383 (1–2) (2004) 213–218.
[29] S. Adhikari, S. Fernando, Hydrogen membrane separation techniques, Industrial & Engineering Chemistry Research 45 (3) (2006) 875–881.
[30] A.L. Greer, Crystallization kinetics of Fe80B20 glass, Acta Metallurgica 30 (1) (1982) 171–192.
[31] A.A. Soliman, et al., Crystallization kinetics of melt-spun Fe83B17 metallic glass, Thermochimica Acta 413 (1–2) (2004) 57–62.
[32] H.F. Li, R.V. Ramanujan, Crystallization behavior of the cobalt based metallic glass Co65Si15B14Fe4Ni2, Materials Science and Engineering A-Structural Materials Properties Microstructure and Processing 375 (2004) 1087–1091.
[33] S.Q. Hao, D.S. Sholl, Using first-principles calculations to accelerate materials discovery for hydrogen purification membranes by modeling amorphous metals, Energy & Environmental Science 1 (1) (2008) 175–183.